

Three-Dimensional Propagation of Kink Wave Trains in Solar Coronal Slabs

Bo Li,¹★ Mingzhe Guo,¹ Hui Yu,¹ Shao-Xia Chen,¹ Mijie Shi¹

¹Shandong Provincial Key Laboratory of Optical Astronomy and Solar-Terrestrial Environment, Institute of Space Sciences, Shandong University, Weihai 264209, China

Accepted XXX. Received YYY; in original form ZZZ

ABSTRACT

Impulsively excited wave trains are of considerable interest in solar coronal seismology. To our knowledge, however, it remains to examine the three-dimensional (3D) dispersive propagation of impulsive kink waves in straight, field-aligned, symmetric, low-beta, slab equilibria that are structured only in one transverse direction. We offer a study here, starting with an analysis of linear oblique kink modes from an eigenvalue problem perspective. Two features are numerically found for continuous and step structuring alike, one being that the group and phase velocities may lie on opposite sides of the equilibrium magnetic field (\mathbf{B}_0), and the other being that the group trajectories extend only to a limited angle from \mathbf{B}_0 . We justify these features by making analytical progress for the step structuring. More importantly, we demonstrate by a 3D time-dependent simulation that these features show up in the intricate interference patterns of kink wave trains that arise from a localized initial perturbation. In a plane perpendicular to the direction of inhomogeneity, the large-time slab-guided patterns are confined to a narrow sector about \mathbf{B}_0 , with some wavefronts propagating toward \mathbf{B}_0 . We conclude that the phase and group diagrams lay the necessary framework for understanding the complicated time-dependent behavior of impulsive waves.

Key words: (Magnetohydrodynamics) MHD - Sun: corona - Sun: magnetic fields - waves

1 INTRODUCTION

The idea of solar coronal seismology (SCS, e.g., Roberts et al. 1984; Uchida 1970) relies heavily on theoretical understandings of magnetohydrodynamic (MHD) waves in structured media. Consequently, there exists an extensive list of studies on MHD waves in both slab and cylindrical equilibria from both eigenvalue problem (EVP) and initial value problem (IVP) standpoints (see e.g., Roberts 2000; Nakariakov & Verwichte 2005; Nakariakov & Kolotkov 2020, for reviews). However, wave trains impulsively excited by localized perturbations seem to be under-examined (see the reviews by e.g., Roberts 2008; Nakariakov et al. 2021), despite their direct involvement in the establishment of SCS (Roberts et al. 1983, 1984). This is particularly true for impulsive kink waves, for which a detailed IVP study was initiated for cylindrical equilibria only recently (Oliver et al. 2014, hereafter ORT14). Equally surprising is the apparent lack of a study on the three-dimensional (3D) propagation of impulsive kink waves in a slab equilibrium, despite the long-lasting interest in EVP studies on oblique kink modes in solar contexts (e.g., Ionson 1978; Wentzel 1979) and despite the literature on IVP studies in 2D (e.g., Murawski & Roberts 1993; Ogrodowczyk & Murawski 2006; Pascoe et al. 2013; Kolotkov et al. 2021; Guo et al. 2022). This manuscript aims at presenting such a study with both an EVP (Section 2) and an IVP (Section 3) approach. We choose to leave out the observational implications, detailing instead how we connect the EVP results, the group diagrams in particular, with our 3D simulation by the method of stationary phase (MSP, Chapter 11 in Whitham

1974, hereafter W74). The group diagrams of 3D kink modes are new to our knowledge, and so is the application of MSP to this context.

2 THE EVP PERSPECTIVE

This section works in zero-beta MHD, involved in which are the mass density (ρ), velocity (\mathbf{v}), and magnetic field \mathbf{B} . Let (x, y, z) denote a Cartesian coordinate system, and let the subscript 0 denote the equilibrium quantities. We consider only static equilibria ($\mathbf{v}_0 = 0$), and take \mathbf{B}_0 to be z -directed and uniform ($\mathbf{B}_0 = B_0 \mathbf{e}_z$). We assume that the equilibrium density (ρ_0) is an even function of x , following

$$\rho_0(x) = \rho_e + \frac{\rho_i - \rho_e}{1 + |x/d|^\alpha}. \quad (1)$$

A continuous profile is chosen to comply with Section 3. Here d represents some slab half-width, and α is some steepness parameter. By “internal” and “external” we refer to the equilibrium quantities at the slab axis ($x = 0$, subscript i) and infinitely far ($|x| \rightarrow \infty$, subscript e), respectively. The internal (external) Alfvén speed v_{Ai} (v_{Ae}) then derives from the internal density ρ_i (external density ρ_e), following $v_A^2 = B_0^2/(\mu_0 \rho_0)$ with μ_0 the magnetic permeability of free space. Only the half-plane $x \geq 0$ needs to be considered. By “out-of-plane” we refer to the y -direction. By “textbook” we refer to the situation where ideal MHD is adopted, out-of-plane propagation is neglected, and $\rho_0(x)$ takes a step profile ($\alpha \rightarrow \infty$, see the textbook by Roberts 2019). An infinity of branches of trapped kink modes arise in this case, and we label a branch by the transverse order $l = 1, 2, \dots$ (e.g., Li et al. 2018, Figure 2). By “kink modes” we restrict ourselves to those that are physically connected to the $l = 1$ textbook modes. We additionally fix $[\rho_i/\rho_e, \alpha]$ at $[3, 10]$ unless stated otherwise.

★ E-mail: bbl@sdu.edu.cn

2.1 Eigenvalue Problem

A linear analysis proves insightful. For prescription (1), however, oblique kink modes are in general resonantly absorbed in the Alfvén continuum unless $\alpha \rightarrow \infty$ (see the review by Goossens et al. 2011, hereafter GER11; also the earliest studies by e.g., Tataronis & Grossmann 1973; Hasegawa & Chen 1974). We adopt a resistive eigenmode approach (see GER11 for conceptual clarifications). Let the subscript 1 denote small-amplitude perturbations, which are Fourier-decomposed as

$$f_1(x, y, z; t) = \Re\{\tilde{f}(x) \exp[-i(\Omega t - k_y y - k_z z)]\}, \quad (2)$$

where Ω is the angular frequency, and k_z (k_y) the real-valued axial (out-of-plane) wavenumber. A much-studied EVP ensues in linear resistive MHD, involving only $\tilde{v}_x, \tilde{v}_y, \tilde{B}_x, \tilde{B}_y,$ and \tilde{B}_z (Goossens et al. 1992; Ruderman et al. 1995; Arregui et al. 2007, A07). The governing equations are identical to Equations (6) to (10) in Yu et al. (2021, Y21). As in Y21, kink eigensolutions are guaranteed by the boundary condition at $x = 0$, namely $d\tilde{v}_x/dx = \tilde{v}_y = d\tilde{B}_x/dx = \tilde{B}_y = \tilde{B}_z = 0$. We require that all Fourier amplitudes vanish at infinity.

The kink eigensolution of interest is unique in that its damping rate becomes independent of the electric resistivity η when η is small enough (see Poedts & Kerner 1991, for the first demonstration). Its η -independent eigenfrequency is formally expressible as

$$\frac{\Omega d}{v_{\text{Ai}}} = \mathcal{W} \left(k_y d, k_z d \left| \frac{\rho_i}{\rho_e}, \alpha \right. \right) = \mathcal{W}(k_y d, k_z d). \quad (3)$$

The second equal sign emphasizes our focus on the k_y - and k_z -dependencies. We follow Y21 to numerically establish \mathcal{W} by solving the EVP with the PDE2D code (Sewell 1988; see Terradas et al. 2006 for its first solar application). Let ω (γ) denote the real (imaginary) part of Ω . Only damping eigensolutions are sought ($\gamma < 0$). Let asterisks denote complex conjugate. The governing equations then dictate that if Ω is an eigenfrequency, then so is $-\Omega^*$. Likewise, if Ω is an eigenfrequency for a given $[k_y, k_z]$, then it remains so for $[-k_y, k_z]$, $[k_y, -k_z]$, and $[-k_y, -k_z]$. It therefore suffices to assume $\omega > 0$ and consider only the quadrant $k_y \geq 0, k_z > 0$.

2.2 Phase and Group Diagrams

This subsection presents the phase and group diagrams. We start by defining a 2D wavevector $\mathbf{k} := k_y \mathbf{e}_y + k_z \mathbf{e}_z$, where $k_y \geq 0$ and $k_z > 0$. The wavevector is alternatively represented by k and θ , with $k = |\mathbf{k}|$ and $\theta = \angle(\mathbf{k}, \mathbf{B}_0)$. We define the phase velocity as $\mathbf{v}_{\text{ph}} = (\omega/k) \mathbf{e}_k$ with \mathbf{e}_k being the unit vector along \mathbf{k} . The group velocity, on the other hand, is defined as $\mathbf{v}_{\text{gr}} = v_{\text{gr},y} \mathbf{e}_y + v_{\text{gr},z} \mathbf{e}_z$ with $v_{\text{gr},y} = \partial\omega/\partial k_y$ and $v_{\text{gr},z} = \partial\omega/\partial k_z$. Equation (3) then enables one to convert the k_y - and k_z -dependencies of $\omega = \Re\Omega$ into the k - and θ -dependencies of \mathbf{v}_{gr} , yielding

$$v_{\text{gr},y}/v_{\text{Ai}} = \mathcal{U}_y(kd, \theta), \quad v_{\text{gr},z}/v_{\text{Ai}} = \mathcal{U}_z(kd, \theta). \quad (4)$$

We largely focus on how \mathbf{v}_{ph} or \mathbf{v}_{gr} varies with θ , for which purpose $\omega, v_{\text{gr},z}$ and $v_{\text{gr},y}$ for the chosen $[\rho_i/\rho_e, \alpha] = [3, 10]$ are plotted against θ by the solid curves in Figures 1a to 1c. A number of kd are examined as labeled. The step results ($\alpha \rightarrow \infty$) are additionally presented by the symbols. One sees that the finite α results differ appreciably from the symbols only for $v_{\text{gr},y}$ when $kd = 1.5$. This is understandable because kink modes with larger k possess shorter spatial scales, and therefore sense the finite inhomogeneity scale more readily. Our point, however, is that the finite α results can be largely understood with the step ones, for which some analytical progress

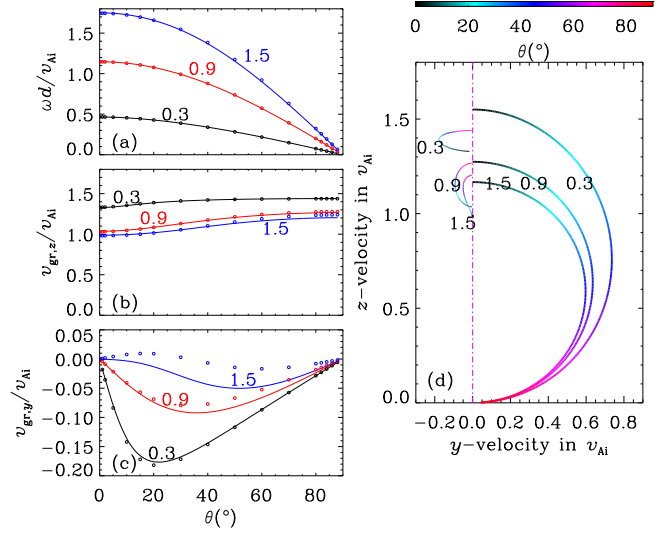


Figure 1. Dispersion properties of oblique kink modes in a slab equilibrium structured only in the x -direction, the density contrast (steepness parameter) being $\rho_i/\rho_e = 3$ ($\alpha = 10$). The obliqueness is measured by the angle θ between the equilibrium magnetic field $\mathbf{B}_0 = B_0 \mathbf{e}_z$ and a 2D wavevector $\mathbf{k} = k_y \mathbf{e}_y + k_z \mathbf{e}_z$. Left column: Dependencies on θ of (a) the oscillation frequency ω , (b) the z -component of the group velocity $v_{\text{gr},z}$, and (c) the y -component $v_{\text{gr},y}$. Several values of kd are examined as labeled. The results for a step density profile ($\alpha \rightarrow \infty$) are represented by the symbols for comparison. Right column: Phase (the thick curves) and group (thin) diagrams for a number of kd as labeled. Both diagrams are color-coded by θ . The dash-dotted line represents the vertical axis in the velocity plane. See text for more details.

is possible. This practice proves necessary given the rather involved θ -dependencies, those of $\mathbf{v}_{\text{gr},y}$ in particular. We proceed to define

$$\kappa_{i,e}^2 = k_z^2 - \frac{\omega^2}{v_{\text{Ai},e}^2}, \quad m_{i,e}^2 = k_y^2 + \kappa_{i,e}^2, \quad (5)$$

where $m_{i,e}$ acts as some effective x -wavenumber for oblique kink modes (e.g., Equation (15) in Y21). We note that m_e^2 is positive by construction, whereas m_i^2 may be negative for small k_y (A07, Figure 2). We take $\arg m_i = \pi/2$ when $m_i^2 < 0$ without loss of generality. A dispersion relation (DR) then writes (e.g., A07; Y21)

$$\coth(m_i d) = -\frac{\kappa_i^2 m_e}{\kappa_e^2 m_i}. \quad (6)$$

The dispersion behavior at large θ can be explained with Equation (6) by assuming $m_i \approx m_e \approx k_y$. It was first shown by Tatsuno & Wakatani (1998) in fusion contexts that

$$\omega \approx k_z C(k_y), \quad C^2(k_y) = v_{\text{Ai}}^2 \frac{1 + \tanh(k_y d)}{\rho_e/\rho_i + \tanh(k_y d)}, \quad (7)$$

which was put in current form by Y21. Note that Equation (7) can also be found by imposing the incompressibility condition from the outset, with the physical reasons well documented for cylindrical equilibria (e.g., Goossens et al. 2009, 2012; Soler & Terradas 2015). Note further that Equation (7) leads to $\kappa_e^2 < |\kappa_i^2|$, meaning that its range of validity $k_y^2 \gg |\kappa_{i,e}^2|$ becomes

$$k_y^2 [\rho_e/\rho_i + \tanh(k_y d)] \gg k_z^2 (1 - \rho_e/\rho_i). \quad (8)$$

Evidently, $\omega \rightarrow 0$ and hence $\mathbf{v}_{\text{ph}} \rightarrow 0$ when $\theta \rightarrow 90^\circ$. Furthermore, one recognizes that $C(k_y)$ decreases monotonically with k_y , meaning that $c_k = v_{\text{Ai}} \sqrt{2/(1 + \rho_e/\rho_i)} < C(k_y) < v_{\text{Ai}} \sqrt{\rho_i/\rho_e} = v_{\text{Ae}}$ with

c_k being the kink speed. Consequently, the asymptotic value of $v_{gr,z}$ at $\theta \rightarrow 90^\circ$ decreases monotonically with k , lying between c_k and v_{Ae} . Likewise, $v_{gr,y}$ approaches zero from below. These step expectations are reproduced exactly by the symbols, explaining the finite α results almost quantitatively as well.

We further employ Equation (6) to understand how $v_{gr,y}$ behaves at small θ . Let $\hat{\omega}$ denote $\mathcal{W}(k_y = 0, k_z)$ (see Equation (3) with $\alpha \rightarrow \infty$). Consider a slightly different pair $[k_y, k_z]$ with $k_y^2/k_z^2 \ll 1$. We see only k_y as variable, and Taylor-expand all terms in Equation (6) about $k_y = 0$. Some lengthy algebra yields that

$$\omega(k_y, k_z) \approx \hat{\omega} \left[1 - \frac{1}{2} \frac{1/(\hat{\kappa}_e d) - 1}{(\hat{\omega} d/v_{Ai})^2 + (k_z d)^2/(\hat{\kappa}_e d)} (k_y d)^2 \right], \quad (9)$$

with $\hat{\kappa}_e$ defined by $\hat{\kappa}_e^2 = k_z^2 - \hat{\omega}^2/v_{Ae}^2$. Note that $\hat{\kappa}_e^2 > 0$. Equation (9) indicates that the k_y -correction is only quadratic, meaning that $v_{gr,y} \rightarrow 0$ when $\theta \rightarrow 0$. For a fixed small θ , one further deduces that $v_{gr,y}$ remains negative for small kd until reversing its sign when kd exceeds some critical value. To explain this, we recall the textbook result that $\hat{\omega}/k_z$ decrease monotonically with k_z from v_{Ae} at $k_z d \rightarrow 0$ toward v_{Ai} when $k_z d \rightarrow \infty$ (e.g., Roberts 2019, Section 5.5.5). Now that $(\hat{\kappa}_e d)^2 = (k_z d)^2 [1 - \hat{\omega}^2/(k_z v_{Ae})^2]$, one recognizes that $\hat{\kappa}_e d \ll 1$ when $k_z d \ll 1$ but increases monotonically with $k_z d$ toward large values when $k_z d \gg 1$. This necessarily changes the sign of $1/(\hat{\kappa}_e d) - 1$ at some $k_z d$, and hence a change of sign of $v_{gr,y}$. Both the curves and symbols in Figure 1c for small θ agree with the analytical expectations. Somehow different between the step and finite α results is that $kd = 1.5$ is large enough to reverse the sign of $v_{gr,y}$ for the former but not for the latter.

Figure 1d gathers the finite α results to produce the phase and group diagrams, namely the trajectories that $\mathbf{v}_{ph} = (v_{ph,y}, v_{ph,z})$ (the thick curves) and $\mathbf{v}_{gr} = (v_{gr,y}, v_{gr,z})$ (thin) traverse when θ varies. These curves are color-coded by θ and labeled by kd . A primary result of this study, Figure 1d is striking in that the trajectories for any examined kd are morphologically similar to slow waves in a uniform low-beta MHD medium, despite the absence of slow waves in zero-beta MHD (see, e.g., Figure 5.4 in Goedbloed et al. 2019). By ‘‘similar’’ we specifically emphasize that \mathbf{v}_{ph} and \mathbf{v}_{gr} lie astride $\mathbf{B}_0 = B_0 \mathbf{e}_z$, and the group trajectories extend only to a limited angle from \mathbf{B}_0 . We deem it important to explore the physical reasons that yield the peculiar group trajectories from the perspective of, say, restoring forces. Equally important is to explore how the group trajectories behave in other configurations, one example being those that are associated with a magnetic shear ($\mathbf{B}_0 = B_{0y}(x)\mathbf{e}_y + B_{0z}(x)\mathbf{e}_z$; see e.g., Chen & Hasegawa 1974; Arregui et al. 2003 for some motivating ideas). These explorations are nonetheless left for a future work.

Figure 2 further surveys an extensive set of $[kd, \theta]$, presenting $v_{gr,y}$ and $v_{gr,z}$ as equally spaced contours colored black and red, respectively. One sees that $v_{gr,y}$ for a given kd consistently approaches zero when $\theta \rightarrow 0$ or $\theta \rightarrow 90^\circ$, thereby attaining a local minimum at some kd -dependent angle θ_{min} . This θ_{min} increases monotonically with kd , and $v_{gr,y}$ is subject to a global minimum in the examined range of kd (see the lower-left portion). Regarding $v_{gr,z}$, one sees that the monotonic θ -dependence for a given kd in Figure 1b actually persists. However, the upper-left corner indicates that $v_{gr,z}$ for a small θ will possess a nonmonotonic kd -dependence when kd further increases. This is indeed true. We avoid this complication, for it is not specific to oblique propagation but well known for $\theta = 0$ when $\alpha \rightarrow \infty$ (e.g., Nakariakov & Roberts 1995). Rather, by Figure 2 we stress that inverting Equation (4) with a given pair $[v_{gr,y}/v_{Ai}, v_{gr,z}/v_{Ai}]$ does not yield a unique pair $[kd, \theta]$.

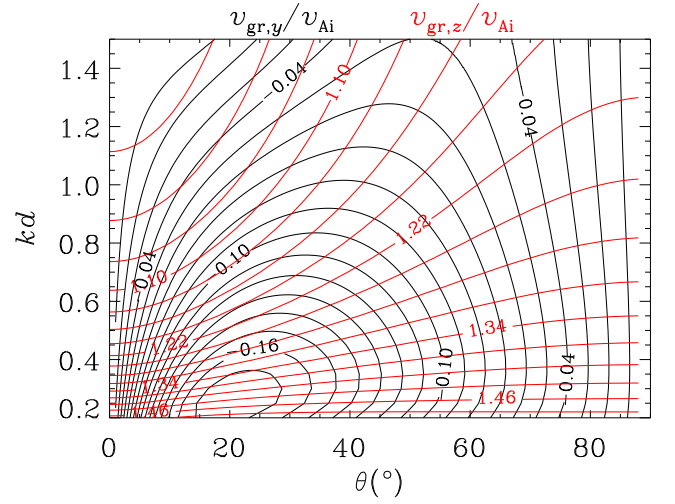


Figure 2. Distributions in the $k - \theta$ plane of the y - and z -components of the group velocity, namely $v_{gr,y}$ (the black contours) and $v_{gr,z}$ (red), for kink modes in a slab equilibrium with $[\rho_i/\rho_e, \alpha] = [3, 10]$.

3 TIME-DEPENDENT SIMULATION

This section examines 3D impulsively excited kink waves by numerically evolving the ideal MHD equations with the MPI-AMRVAC code (Xia et al. 2018). We prescribe the equilibrium density ρ_0 by Equation (1) with $[\rho_i/\rho_e, \alpha] = [3, 10]$. A uniform temperature T_0 is specified for simplicity, yielding a plasma beta of 0.021 at $x = 0$. We choose a z -directed magnetic field \mathbf{B}_0 whose magnitude varies with x to maintain transverse force balance. This x -variation is nonetheless very weak, with B_0 at large x being larger than that at $x = 0$ by only $\sim 0.7\%$. Kink waves are excited by a perturbation

$$v_x(x, y, z; t = 0) = v_{ini} \exp\left(-\frac{x^2}{2\sigma_x^2}\right) \exp\left(-\frac{y^2}{2\sigma_y^2}\right) \exp\left(-\frac{z^2}{2\sigma_z^2}\right), \quad (10)$$

for which the spatial extent is chosen to be $\sigma_x = \sigma_y = \sigma_z = \sqrt{2}d$ and the magnitude v_{ini} is set to be $0.1v_{Ai}$. Note that the same equilibrium was employed in the 2D study by Guo et al. (2022), and Figure 4 therein demonstrated that a magnitude $v_{ini} = 0.1v_{Ai}$ ensures a linear behavior for the resulting kink wave train. No nonlinearity is discerned in this 3D study either, which is understandable given that nonlinearity is weaker with the introduction of the third dimension.

Our numerical setup is as follows. A subdomain $[-50, 50]d \times [0, 200]d \times [0, 200]d$ of the full space is employed from symmetry considerations, with symmetric boundary conditions (BCs) specified at $y = 0$ and $z = 0$. Outflow BCs are implemented for the rest of the boundaries, where no spurious wave reflection is discerned. We adopt the second-order HLLD solver and the Woodward slope limiter when evaluating inter-cell fluxes, and choose the midpoint method for time marching with a Courant number of 0.5. A base grid of $64 \times 128 \times 128$ is adopted in (x, y, z) . Four levels of adaptive mesh refinement (AMR) are implemented as triggered by density and velocity variations, resolving scales down to $\sim 0.19d$. Despite the symmetry considerations and the implementation of AMR, this simulation remains computationally expensive, and the chosen $\alpha = 10$ is the largest we can afford to avoid spurious waves emanating from the slab boundaries.

Figure 3 presents several snapshots of v_x in the $y = 0$ (the left column) and $x = 0$ planes (right). The $y = 0$ cuts, together with the associated animation, make it clear that the signals comprise a slab-guided component and a laterally propagating component. This lat-

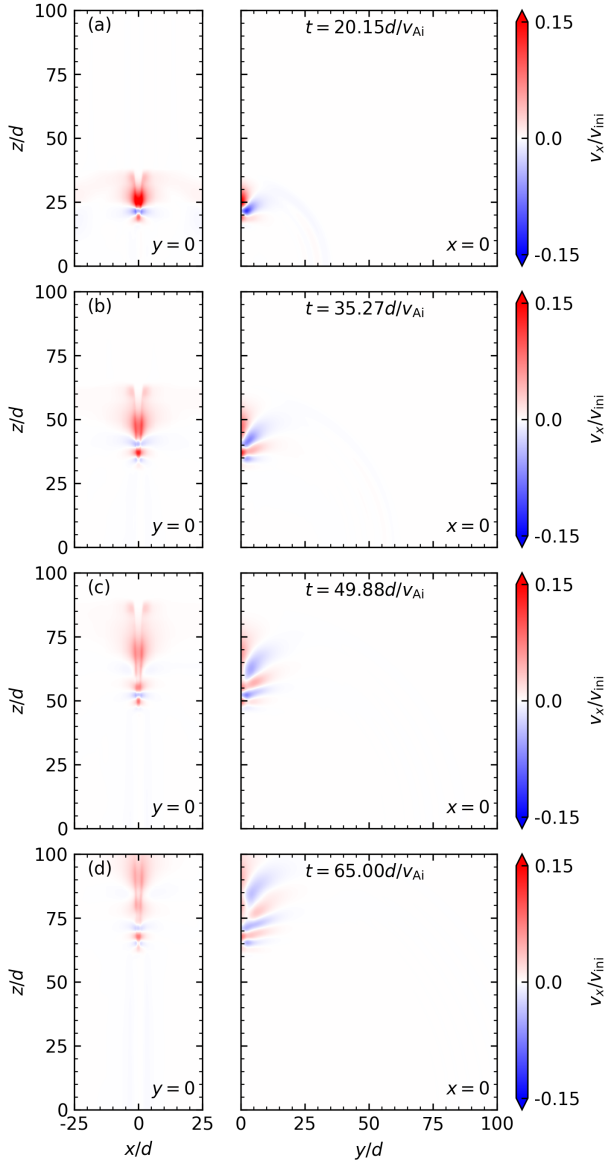


Figure 3. Snapshots of v_x in the $y = 0$ (the left column) and $x = 0$ (right) planes. These images are extracted from the animation attached to this figure.

eral component, manifested as a series of circular ripples, attenuates rather rapidly and becomes difficult to discern when $t \gtrsim 30d/v_{Ai}$. In contrast, the guided component persists throughout, characterized by that more ripples emerge with time and that small-scale variations tend to lag behind larger-scale ones. Two features arise in the $x = 0$ cuts. First, the nominal lateral component is present as well, despite that the $x = 0$ plane is inside the slab. Second, the guided component is confined to a rather narrow sector about \mathbf{B}_0 , encompassing multiple stripes that form an intricate interference pattern.

We focus on the $x = 0$ cuts, for the $y = 0$ patterns are largely 2D (Guo et al. 2022, Figure 4). Neglecting finite pressure, we assume $\alpha \rightarrow \infty$ to make quantitative progress. One may write

$$v_x(x, y, z, t) = \int_{-\infty}^{\infty} dk_y \int_{-\infty}^{\infty} dk_z \left\{ \sum_j \left[\mathcal{F}_j(x; k_y, k_z) e^{i(\omega_j t - k_y y - k_z z)} \right] + \text{improper} \right\}, \quad (11)$$

by drawing analogy with the cylindrical study by ORT14 (see also Li et al. 2022). A spectral solution to the IVP, Equation (11) means that all values of k_y and k_z are involved given the localization of the initial perturbation. The summation collects all trapped modes, for which the frequency $\omega_j = \omega_j(k_y, k_z)$ ensures $m_e^2 > 0$ (see Equation (5)). The “improper” part incorporates improper modes, which possess any frequency satisfying $m_e^2 < 0$ and hence necessitate an integration over frequency. Regardless, the “lateral” component in Figure 3 is attributable to the improper contribution.

We now consider the guided component by connecting Equation (11) with the resistive EVP results encapsulated in Figures 1 and 2. Before proceeding, however, the following remarks are necessary. Firstly, the group velocity v_{gr} involves only the real part (ω) of the eigenfrequency Ω . What a non-vanishing $\gamma = \Im\Omega$ means for an ideal computation is that the fast wave energy is transferred to localized Alfvénic motions where the Alfvén resonance takes place, as has been extensively demonstrated for kink modes in cylindrical equilibria (e.g., Terradas et al. 2008; Pascoe et al. 2010; Soler & Terradas 2015). The same also happens here in that Alfvénic motions can be readily discerned as enhanced velocity shear $\partial v_y / \partial x$ in some moving volumes in the slab boundary that accompany the strongest v_x perturbations. Secondly, strictly speaking, our EVP analysis needs to account for the finite beta to ensure a more self-consistent application of the EVP computation to the IVP study. On top of that, implied by such an application is that resonant absorption does not significantly impact the oscillation frequency ω , which may not hold in general (Soler & Terradas 2015). Nonetheless, two reasons make us believe that this is not too serious an issue, one being that $|\gamma/\omega|$ is consistently < 0.1 for the wavevectors examined in Figure 2, the other being related to some quantitative analysis in what follows.

Figures 4a and 4b present two zoomed-in $x = 0$ cuts of v_x . A portion of the outermost $v_x = 0$ contour is given. With this iso-phase curve we illustrate the relevance of Figure 1d to the large-time interference pattern. Key is that the method of stationary phase (MSP) is increasingly applicable as time proceeds. Suppose that the MSP applies to some (y, z, t) . Equation (11) is then dominated by those wavepackets (WPs) with central wavevectors $\mathbf{K}_n = K_{n,y} \mathbf{e}_y + K_{n,z} \mathbf{e}_z$ (W74, Equation (11.41)),

$$v_x(0, y, z, t) \sim t^{-1} \sum_n \left[\mathcal{G}_n(K_{n,y}, K_{n,z}) e^{i(\omega_n t - K_{n,y} y - K_{n,z} z)} \right], \quad (12)$$

where $\omega_n = \omega_n(\mathbf{K}_n)$ with \mathbf{K}_n a solution to

$$v_{gr,y}(\mathbf{K}_n) = y/t, \quad v_{gr,z}(\mathbf{K}_n) = z/t. \quad (13)$$

One complication, however, is that Equation (13) possesses two solutions even if one assumes the relevance of only those modes in Figure 2. This is illustrated in Figure 4a where the arrows represent the central wavevectors of the two WPs that solve Equation (13) for a point with $y = 4d$ on the $v_x = 0$ curve. Note that $K_y < 0$ (see the symmetry property following Equation (3)). Let these WPs be labeled 1 and 1', and suppose that the unprimed WP dominates. Two consequences follow. First, \mathbf{K}_1 is locally normal to the iso-phase curve. Second, the time sequence seen by WP 1, $V_x(t) := v_x(0, v_{gr,y}(\mathbf{K}_1)t, v_{gr,z}(\mathbf{K}_1)t, t)$, eventually becomes $\sim t^{-1} \sin[\varpi(\mathbf{K}_1)t + \phi(\mathbf{K}_1)]$ with

$$\varpi(\mathbf{K}_1) = \omega(\mathbf{K}_1) - K_{1,y} v_{gr,y}(\mathbf{K}_1) - K_{1,z} v_{gr,z}(\mathbf{K}_1) \quad (14)$$

being a Doppler-shifted frequency and ϕ some phase angle. This second property applies to any WP, and is hence useful for assessing whether the MSP applies or judging whether a WP dominates. The

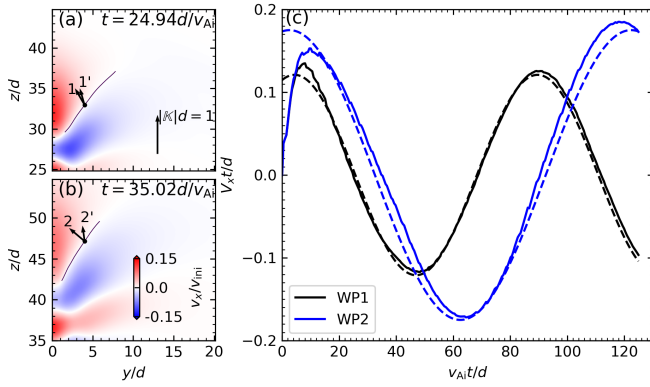


Figure 4. Left: Snapshots of v_x in the $x = 0$ plane at two labeled instants. The solid curve in each panel is part of the outermost $v_x = 0$ contour, the arrows representing the central wavevectors of the two wavepackets expected for the location chosen on this iso-phase curve. The vertical arrow measures the magnitude of any wavevector. Right: The time sequence of $v_x t$ sampled by wavepacket 1 (the black solid curve) or wavepacket 2 (blue). Each sequences is fitted with a sinusoid incorporating expectations from linear theory (the dashed curve). See text for details.

$V_x(t)t$ sequence seen by WP 1 is presented by the black solid curve in Figure 4c. A sinusoid fitting with the expected $\varpi(\mathbf{K}_1)$ (the black dashed curve) strongly suggests that the MSP applies to the trajectory of WP 1 when $t \gtrsim 7d/v_{Ai}$, despite the minor deviation of \mathbf{K}_1 from the local normal. The same practice is repeated for WP 2 in Figure 4b pertinent to a point with $y = 4d$ on the solid curve. Now the MSP applies for $t \gtrsim 10d/v_{Ai}$ (see the blue curves in Figure 4c), and \mathbf{K}_2 is nearly perfectly perpendicular to the iso-phase curve. The negative y -propagation of the delineated $v_x = 0$ front may therefore be accounted for by the dispersion features in Figure 1d.

4 SUMMARY

This study examined the three-dimensional (3D) propagation of kink wave trains impulsively excited by a localized perturbation to straight, field-aligned, symmetric, coronal slabs that are structured only in one transverse direction. Two features stand out in our linear EVP analysis on oblique kink modes, namely the group and phase velocities may lie astride the equilibrium magnetic field (\mathbf{B}_0), and the group trajectories extend only to a limited angle from \mathbf{B}_0 . These features were demonstrated numerically for continuous and step structuring alike, and were understood with the approximate analytical expressions enabled by the latter. Our 3D time-dependent simulation showed that these features are reflected in the intricate interference patterns at large times, the key being the ideas behind the method of stationary phase. The guided wave trains in the out-of-plane cut through the slab axis are confined to a narrow sector about \mathbf{B}_0 , with some wavefronts propagating toward \mathbf{B}_0 .

ACKNOWLEDGEMENTS

We thank the referee (Dr. Roberto Soler) for constructive comments. This research was supported by the National Natural Science Foundation of China (41974200, 41904150, and 11761141002). We gratefully acknowledge ISSI-BJ for supporting the international team ‘‘Magnetohydrodynamic wavetrains as a tool for probing the solar corona’’.

DATA AVAILABILITY

The data underlying this article are available in the article and in its references.

REFERENCES

- Arregui I., Oliver R., Ballester J. L., 2003, *A&A*, **402**, 1129
 Arregui I., Terradas J., Oliver R., Ballester J. L., 2007, *Sol. Phys.*, **246**, 213
 Chen L., Hasegawa A., 1974, *Physics of Fluids*, **17**, 1399
 Goedbloed H., Keppens R., Poedts S., 2019, *Magnetohydrodynamics of Laboratory and Astrophysical Plasmas*. Cambridge University Press, doi:10.1017/9781316403679
 Goossens M., Hollweg J. V., Sakurai T., 1992, *Sol. Phys.*, **138**, 233
 Goossens M., Terradas J., Andries J., Arregui I., Ballester J. L., 2009, *A&A*, **503**, 213
 Goossens M., Erdélyi R., Ruderman M. S., 2011, *Space Sci. Rev.*, **158**, 289
 Goossens M., Andries J., Soler R., Van Doorselaere T., Arregui I., Terradas J., 2012, *ApJ*, **753**, 111
 Guo M., Li B., Van Doorselaere T., Shi M., 2022, *MNRAS*, **515**, 4055
 Hasegawa A., Chen L., 1974, *Phys. Rev. Lett.*, **32**, 454
 Ionson J. A., 1978, *ApJ*, **226**, 650
 Kolotkov D. Y., Nakariakov V. M., Moss G., Shellard P., 2021, *MNRAS*, **505**, 3505
 Li B., Guo M.-Z., Yu H., Chen S.-X., 2018, *ApJ*, **855**, 53
 Li B., Chen S.-X., Li A.-L., 2022, *ApJ*, **928**, 33
 Murawski K., Roberts B., 1993, *Sol. Phys.*, **144**, 101
 Nakariakov V. M., Kolotkov D. Y., 2020, *ARA&A*, **58**, 441
 Nakariakov V. M., Roberts B., 1995, *Sol. Phys.*, **159**, 399
 Nakariakov V. M., Verwichte E., 2005, *Living Reviews in Solar Physics*, **2**, 3
 Nakariakov V. M., et al., 2021, *Space Sci. Rev.*, **217**, 73
 Ogradowczyk R., Murawski K., 2006, *Sol. Phys.*, **236**, 273
 Oliver R., Ruderman M. S., Terradas J., 2014, *ApJ*, **789**, 48
 Pascoe D. J., Wright A. N., De Moortel I., 2010, *ApJ*, **711**, 990
 Pascoe D. J., Nakariakov V. M., Kupriyanova E. G., 2013, *A&A*, **560**, A97
 Poedts S., Kerner W., 1991, *Phys. Rev. Lett.*, **66**, 2871
 Roberts B., 2000, *Sol. Phys.*, **193**, 139
 Roberts B., 2008, in Erdélyi R., Mendoza-Briceno C. A., eds, Vol. 247, *Waves & Oscillations in the Solar Atmosphere: Heating and Magnetoseismology*. pp 3–19, doi:10.1017/S1743921308014609
 Roberts B., 2019, *MHD Waves in the Solar Atmosphere*. Cambridge University Press, doi:10.1017/9781108613774
 Roberts B., Edwin P. M., Benz A. O., 1983, *Nature*, **305**, 688
 Roberts B., Edwin P. M., Benz A. O., 1984, *ApJ*, **279**, 857
 Ruderman M. S., Tirry W., Goossens M., 1995, *Journal of Plasma Physics*, **54**, 129
 Sewell G., 1988, *The Numerical Solution of Ordinary and Partial Differential Equations*. San Diego: Academic Press
 Soler R., Terradas J., 2015, *ApJ*, **803**, 43
 Tataronis J., Grossmann W., 1973, *Zeitschrift fur Physik*, **261**, 203
 Tatsuno T., Wakatani M., 1998, *Journal of the Physical Society of Japan*, **67**, 2322
 Terradas J., Oliver R., Ballester J. L., 2006, *ApJ*, **642**, 533
 Terradas J., Andries J., Goossens M., Arregui I., Oliver R., Ballester J. L., 2008, *ApJ*, **687**, L115
 Uchida Y., 1970, *PASJ*, **22**, 341
 Wentzel D. G., 1979, *ApJ*, **227**, 319
 Whitham G., 1974, *Linear and Nonlinear Waves*. New York: Wiley, <https://books.google.nl/books?id=f8oRAQAATAA>
 Xia C., Teunissen J., El Mellah I., Chané E., Keppens R., 2018, *ApJS*, **234**, 30
 Yu H., Li B., Chen S., Guo M., 2021, *Sol. Phys.*, **296**, 95

This paper has been typeset from a \LaTeX file prepared by the author.